Inorganic Chemistry

pubs.acs.org/IC
Article

Role of Transition Metal Dichalcogenides as a Catalyst Support for Decorating Gold Nanoparticles for Enhanced Hydrogen Evolution Reaction

Boontarika Saeloo, Thanit Saisopa, Panwad Chavalekvirat, Pawin Iamprasertkun, Kulpavee Jitapunkul, Weekit Sirisaksoontorn, T. Randall Lee, and Wisit Hirunpinyopas*

Cite This: *Inorg. Chem.* 2024, 63, 18750−18762

ABSTRACT: The two-dimensional (2D) transition metal dichalcogenides (TMDs) have been widely used in various electrochemical applications, such as electrocatalysts, sensors, and energy storage. They have been potentially demonstrated not only as catalysts but also as supporting materials for boosting catalytic performance and durability. However, the different types of TMD nanosheets (transition metals and chalcogenide atoms) for supporting nanoparticles have not yet been investigated for electrocatalytic performance. Herein, we provide mechanistic insights into the hydrogen evolution reaction (HER) of various TMDs (i.e., MoS_2, $MoSe_2$, and WSe_2) as catalyst supports for the decoration of gold nanoparticles (AuNPs), which represent an active catalyst. Among various TMD supports, it was found that the MoS_2 supports with an optimal amount of AuNPs loading (MoS_2/AuNPs) exhibited excellent catalytic activity (low overpotential and Tafel slope), which is better than that of other TMD supports and the previously reported TMD-based support. This is due to well-dispersed AuNPs with the charge transfer of Au-MoS_2 interaction (increasing *n*-type), leading to highly active sites for HER performance. Moreover, the perfect laminar stacking of the MoS_2/AuNPs electrode, providing high porosity and good wettability, plays an important role in enhancing the ability of ionic electrolytes to infiltrate through the electrode area (up to ∼50 F g^{-1}). The MoS_2/AuNPs exhibit long-term stability with no disintegration of the electrode when performing the HER at ultrahigh current density (>200 mA cm^{-2}) for over 24 h. This work aims to deepen the understanding of TMD materials as catalyst supports, and is advantageous for the development of catalyst-based applications.

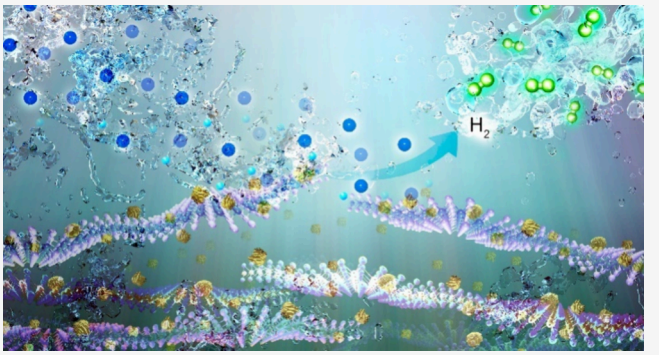

1. INTRODUCTION

Transition metal dichalcogenides (TMDs; MoS_2, $MoSe_2$, WSe_2, etc.) is one of two-dimensional (2D) materials, which chemical formula is MX_2; where M is transition metals (Mo, W, V, etc.) and X is chalcogen atoms (S, Se, etc.). The structure of a monolayer TMD nanosheet consists of a three-atom thickness in which a transition metal atom is sandwiched between two chalcogen atoms via a covalent bond. The 2D TMD nanosheet can be easily exfoliated via a weak van der Waals force between individual layers, providing a number of active sites. The TMDs have been attractive due to various promising properties such as ultrahigh specific surface area, mechanical strength, and flexibility.[1,2] The TMD-based materials have been demonstrated as sustainable keys in a wide range of applications such as electronic devices,[3] energy storage,[4,5] membrane-based filtration,[6,7] and catalysis,[8,9] Especially, the use of TMD nanosheets has been widely applied as alternative electrocatalyst and catalyst support for enhanced catalytic performance.[10−15]

Currently, one of the alternative energy sources demanding high energy efficiency, sustainability, and environmentally friendly energy sources is hydrogen energy. This can be generated by electrolytic water splitting, so-called the hydrogen evolution reaction (HER).[16−18] In general, platinum (Pt)-based catalysts play the most important role in electrocatalysts for HER due to the optimal hydrogen chemisorption energy (volcano plots).[19,20] In fact, Pt has been limited for industrial-scale production due to high cost, scarcity, and fast degeneration. The 2D TMD, being a non-noble metal, has attracted great interest in replacing Pt-based catalysts due to low cost, high chemical stability, and excellent electrocatalytic

Received: June 27, 2024
Revised: September 13, 2024
Accepted: September 18, 2024
Published: September 27, 2024

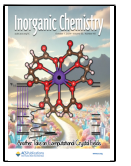

https://doi.org/10.1021/acs.inorgchem.4c02668
Inorg. Chem. 2024, 63, 18750−18762

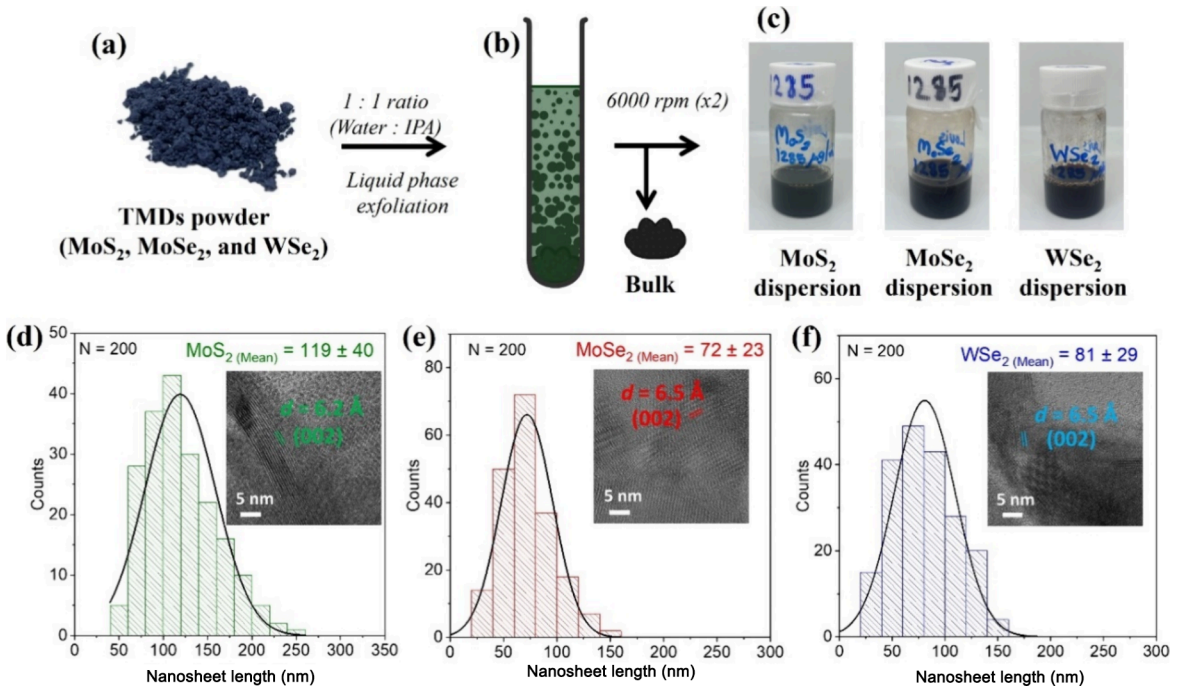

Figure 1. Preparation of each TMD dispersion. (a) Schematic illustration of the preparation of TMD dispersion via bath sonication process. (b) Schematic showing the collection of TMD dispersions using a centrifugation method. (c) Photographs of concentrated MoS_2, $MoSe_2$, and WSe_2 dispersions at an identical concentration with their corresponding size histograms showing in (d–f) as measured by statistical TEM. Insets in (d–f) show HR-TEM with their *d*-spacing.

activity, which can potentially be alternative HER catalysts.[21−23] However, the catalytic performance of pristine exfoliated TMDs is still far lower than that of the precious noble metals. To achieve highly efficient catalytic reactions, the structural modifications of exfoliated TMD materials have been demonstrated, for example, chemical functionalization,[6,24] metal deposition or doping (e.g., Pt, MoP, and Ru),[11−13,15,25] composite materials (e.g., $CoSe_2$ and MoO_2)[26−28] phase transformation (semiconductive 2H to conductive 1T MoS_2),[23] and so on. Therefore, the particular modifications of exfoliated TMD materials are considered to be an efficient route to boost the highly exposed catalytic sites and thus contribute to excellent HER activity.

Among those methods, the catalytic TMD performances can be simply modified by deposition of the metal catalyst. As a result, the surface modifications of TMDs with metal decoration can effectively not only improve electron transfer but also increase the exposed active sites.[11,13] Several studies have shown that nanoparticles decorated on the active surface of 2D TMD nanosheets can significantly promote HER activity. For example, there have been reported 2D TMDs (e.g., MoS_2, $MoSe_2$, WSe_2, etc.) as support for depositing nanoparticles (i.e., Pt, Pd, and Rh) for enhanced catalytic activity.[13,14,27,29] The results indicate that the increase in catalytic HER performance results from the synergistic catalytic effects between nanoparticles and TMD supports, which is still unclear, particularly in electronic interaction among metal deposition and TMD supports. In addition, among various TMD materials, the suitable one as a catalyst support has not been prior investigated. This could disclose the mechanistic insights into a TMD-based catalyst for decorating nanoparticles as well as the role of TMD supports for advanced catalyst-based applications.

In this work, we have prepared 2D transition metal dichalcogenide (TMD) dispersions (i.e., MoS_2, $MoSe_2$, and WSe_2) by facile liquid-phase exfoliation using a low and safe chemical process. The as-prepared TMD nanosheets were used as a supporting material for decorating gold nanoparticles (AuNPs) as electrocatalysts for HER activity. The TMD/AuNPs electrodes were characterized using various physical and electrochemical techniques, particularly X-ray photoelectron spectroscopy, to observe the change in their electronic structures. The addition of AuNPs on TMD supports was finely tuned to obtain the optimal conditions. We found that MoS_2 nanosheets behaved with great AuNPs support (MoS_2/AuNPs), exhibiting excellent HER performance. This was due to a number of highly exposed active sites of AuNPs on MoS_2 supports with charge transfer from the AuNPs to the MoS_2 materials. Furthermore, the charge storage contributions leading to the electrochemically active surface area of as-prepared TMD/AuNPs were also determined for both areal and gravimetric capacitances to disclose the physical mechanism of TMD supports. Also, the MoS_2/AuNPs electrode was performed at ultrahigh current density (>200 mA cm^{-2}) for a long period of time to determine the long-term stability of the as-prepared electrode, which could demonstrate real-world industrial applications.

2. EXPERIMENT

2.1. Materials. Molybdenum disulfide (99%, MoS_2), molybdenum diselenide (99%, $MoSe_2$), tungsten diselenide (99%, WSe_2), isopropanol, gold nanoparticles (5 nm diameter with highly monodisperse, ~5.5 × 10^{13} particles mL^{-1}, stabilized in citrate buffer), and Nafion perfluorinated resin solution (5 wt % in a mixture of lower aliphatic alcohols and water) were purchased from Sigma-Aldrich. Glassy carbon disk electrodes (3 mm diameter) were purchased from PalmSens.

https://doi.org/10.1021/acs.inorgchem.4c02668
Inorg. Chem. 2024, 63, 18750−18762

Omnipore membrane filters (polyvinylidene fluoride, PVDF, hydrophilic surface, 0.1 μm pore size) were purchased from Merck Millipore Limited. Ultrapure deionized water (Milli Q water) was used in all aqueous solution preparation.

2.2. Preparation of TMD Dispersions. The transition metal dichalcogenide (TMD) dispersion was prepared by the liquid-phase exfoliation (LPE) technique under a bath sonication process. This technique has been widely used in several electrochemical applications.[30] Shortly, 1 g of TMD powder (i.e., MoS_2, $MoSe_2$, and WSe_2) was sonicated in 100 mL of a mixed solvent (ultrapure water/isopropanol in 1:1 ratio) at a frequency of 37 kHz and a power of 300 W for 12 h at 25 °C (Figure 1a). The obtained dispersion was centrifuged twice at 6000 rpm for 30 min, collecting at the top 80% of supernatant to avoid unexfoliated materials, as shown in Figure 1b. Then, the concentration of the exfoliated TMD dispersion was increased by a mild rotary evaporation process at 40 °C. This can facilitate the sample preparation on a glassy carbon electrode.[31] To determine the TMD concentration, the dispersions were filtered through PVDF filters. The PVDF filter should be weighted with a 5-decimal analytical balance to minimize errors in measurement. The obtained TMD films on the PVDF filter were dried in an oven overnight and reweighted to obtain the actual TMD mass. This process was repeated at least 3 times to obtain the average concentration. All TMD dispersions were adjusted to be identical concentrations (1.28 mg mL^{-1}) for electrode preparation (see Figure 1c). The nanosheet distribution of obtained TMD dispersions was determined using dynamic light scattering (DLS). It was shown that the nanosheet distribution of each TMD is well-distributed with a corresponding nanosheet size of a few hundred nanometers (see Figure S1). No uncommon hazards were noted during the TMD preparation.

2.3. Characterization of TMD Dispersions and TMD/AuNPs. *2.3.1. TMD, Gold Colloid, and TMD/AuNP Dispersions.* The size distribution and zeta potential of each TMD dispersion were determined by dynamic light scattering (DLS) using a Malvern Zetasizer Nano ZS with Zetasizer software. A 633 nm He−Ne laser was used to measure the lateral size of the TMD nanosheets in a square glass cuvette. The zeta potential of each TMD dispersion was measured in a disposable folded capillary. Moreover, transmission electron microscopy (TEM; JEOL JEM-2010F) was carried out to determine the direct TMD nanosheet sizes and the distribution of AuNPs on the TMD support. The dispersions were diluted in 2-propanol alcohol to minimize the effect of nanosheet aggregation. The samples were prepared on a carbon copper grid and dried in a vacuum oven.

2.3.2. Pristine TMD and TMD/AuNP Electrodes. A scanning electron microscope (SEM; FEI Quanta 450 FEG) was performed with an accelerating voltage of 15 kV under a high vacuum to observe the electrode morphology. X-ray diffraction (XRD; Bruker D8 ADVANCE diffractometer) was performed for the phase identification of each TMD/AuNPs electrode. The XRD patterns were obtained using a Cu−Kα radiation source at a wavelength of 1.5406 Å in the range 2θ of 5−70° with a step size of 0.02° s^{-1}. The structure of each TMD was also determined by Raman spectroscopy using the HORIBA XploRA PLUS instrument. Raman spectra were recorded in the range between 200 and 500 cm^{-1} using a 532 nm laser (2.33 eV) and a laser power of 0.1% with a grating of 1800 l/mm. The optical images were taken with a 50× objective lens.

2.3.3. Electrochemical Measurement. For electrode preparation, 50 μL of each TMD dispersion (1.28 mg mL^{-1}) was mixed with ∼2 μL of Nafion solution. Then, the TMD solution was added with gold colloid (AuNPs; 5 nm diameter, ∼ 5.5 × 10^{13} particles mL^{-1}) as a function of volume (10−500 μL). The mixed solution was dropped on a polished glassy carbon electrode (GCE: area = 0.071 cm^2) and dried at 55 °C in an oven, which was used as a working electrode. The TMD loading on a GCE was controlled at 30 μg cm^{-2} for all electrodes, and the amount of AuNPs is in the range from 1.82 × 10^9 to 9.12 × 10^{11} particles. Note that pristine AuNP samples (10−500 μL) were prepared using 50 μL of a mixture of isopropanol and water (1:1 v/v) for comparison. The effect of catalyst loading on a GCE (5−60 $\mu g/cm^2$) is presented in the Supporting Information.

The electrocatalytic performance of each sample was carried out under a three-electrode system using a potentiostat (PGSTAT302N, Methrohm Autolab, The Netherlands) at room temperature. The reference and counter electrodes were the standard double-junction silver/silver chloride (Ag/AgCl in 3 M KCl) and platinum (Pt) electrodes, respectively. All electrochemical measurements were conducted under aqueous 0.5 M H_2SO_4. The electrolyte was purged by nitrogen gas for over 30 min prior to measurement. The linear sweep voltammogram (LSV) technique was used to determine the kinetic of the HER reaction with a scan rate of 5 mV s^{-1} during a potential range of 0 to −1 V (versus reversible hydrogen electrode; RHE). Tafel plot and the overpotential at 10 mA cm^{-2} were used to estimate the mechanism and catalytic activity. Charge transfer resistance (R_{ct}) of each TMD/AuNPs was obtained using electrochemical impedance spectroscopy (EIS) with an applied potential of −0.3 V (vs RHE) at an amplitude of 10 mV in a frequency range of 0.01−10^5 Hz. For all measurements, the potentials were calibrated using the reversible hydrogen electrode (RHE) using the following equation: $E_{(RHE)} = E_{(Ag/AgCl)} + 0.207 + 0.0591pH$. All polarization curves were corrected by iR drop corrections with 90% solution resistance.

Cyclic voltammetry (CV) was used to determine the double-layer capacitance (C_{dl}) of as-prepared TMD/AuNPs electrodes. The CV profiles were recorded in a nonfaradaic potential window between 0.55 and 0.75 V (vs RHE) with various scan rates of 0.5−200 mV s^{-1}. To determine double-layer capacitance, the specific capacitance of each TMD/AuNPs can be calculated using the integral of CV with the equation

$$C_s = \int \frac{I dV/v}{m\Delta V}$$

where m is the mass of the electrocatalyst on GCE (g), v is the scan rate (V s^{-1}), and ΔV is the potential range in the discharge range (V). The electrocatalyst stability was examined by LSV before and after CV for 5,000 cycles with a potential range from 0.55 to 0.75 V (vs RHE) at a scan rate of 100 mV s^{-1}. The stability was also tested at ultrahigh current density using a time-dependent technique at applied potentials of −0.25 and −0.75 V (vs RHE) for over 24 h.

3. RESULTS AND DISCUSSION

3.1. pristine TMD and TMD/AuNP Electrodes. The lateral size of TMD nanosheets was directly measured using statistical analysis as obtained from transmission electron

https://doi.org/10.1021/acs.inorgchem.4c02668
Inorg. Chem. 2024, 63, 18750−18762

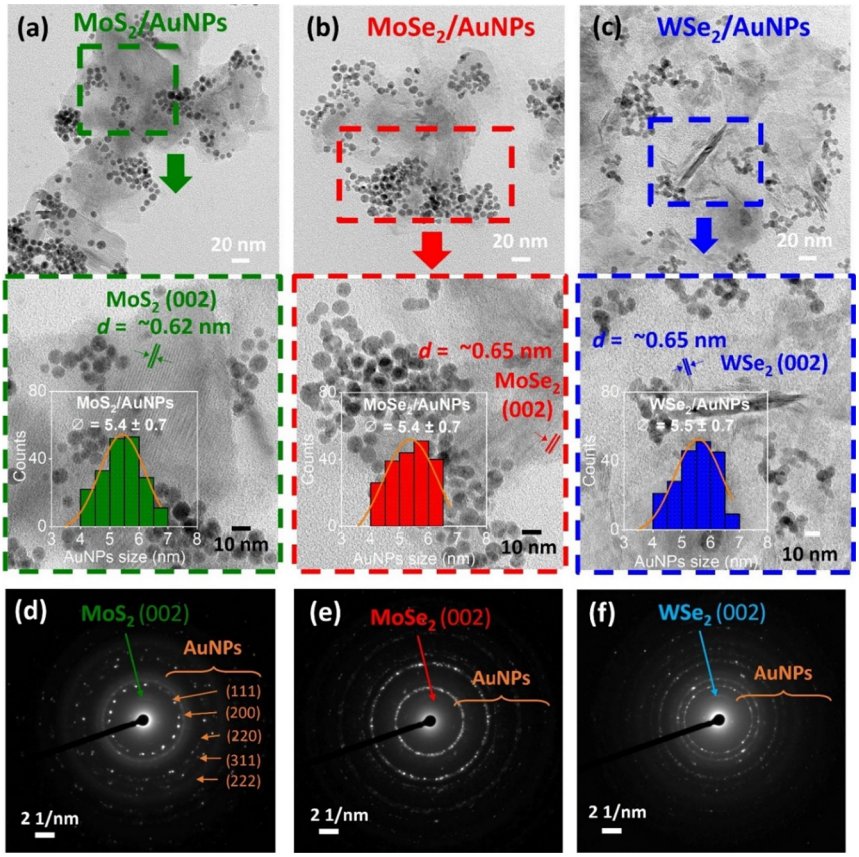

Figure 2. AuNPs distribution on each TMD nanosheet. TEM images and their enlarged (a) MoS_2/AuNPs, (b) $MoSe_2$/AuNPs, and (c) WSe_2/AuNPs. Inset in parts (a–c) show the size distribution of AuNPs on TMD supports. (d–f) Corresponding SAED images.

microscopy (TEM) data (Figure S2a–c). The plots of size distribution for each TMD with high-resolution TEM images are shown in Figure 1d–f. It was found that the average lateral size of MoS_2 is slightly larger than that of the others. However, as the TMD dispersions consist of a variety of nanosheet sizes, the size distribution of each TMD obtained is still in a similar range (50–200 nm), which was in comparable nanosheet sizes for this study.

Figure 2a–c shows the TEM images of MoS_2/AuNPs, $MoSe_2$/AuNPs, and WSe_2/AuNPs, respectively, exhibiting a distribution of AuNPs on each TMD nanosheet with their enlarged TEM images. The samples were prepared under the optimal conditions between TMD support and the amount of AuNPs loading as the excellent catalytic performance, which corresponds to $\sim 4.56 \times 10^{11}$ particles on a constant 2.13 μg of TMD support (30 μg cm^{-2} on a working electrode). The amount of AuNPs on a GCE could be calculated when the concentrations of TMD (1.28 mg mL^{-1}) and colloidal gold ($\sim 5.5 \times 10^{13}$ particles mL^{-1}) were known (see Table S1 in the Supporting Information). Due difference in structural compositions of 2D TMDs contributes to characteristic physical (lateral size and thickness) and electronic properties (surface charge and conductivity), this plays a crucial role in the AuNPs distribution on each TMD support. As a result, it was found that the decoration of AuNPs on MoS_2 nanosheets was greater than that of the others, owing to a high basal-to-edge ratio for the MoS_2 support. The size distributions of AuNPs on each TMD nanosheet (see Figure 2a–c: inset) were measured to be in the range of 4–7 nm with the mean particle size of 5.4 ± 0.7 nm, indicating a well-uniformed particle size on TMD supports. This analysis agrees well with the product specification of colloidal gold (5 nm diameter). Not only the distribution of AuNPs on TMD supports was shown, but a particular interaction between the AuNPs and TMD supports was also raised (discussed in XPS analysis). In addition, the interaction between AuNPs and TMD support can correlate to surface charge properties, as measured by ζ-potentials. The strong electrostatic repulsion between the highly negative charge of AuNPs (−38.8 mV) and both $MoSe_2$ (−34.1 mV) and WSe_2 (−33.7 mV) can occur, while it has a small impact on MoS_2 (−23.3 mV). This can result in a difference in the amount of AuNPs on TMD supports (discussed in XRF and EDS analyses). Moreover, the selected area electron diffraction (SAED) patterns were used to identify the compositions of the TMD/AuNPs, as shown in Figure 2d–f. It was clearly seen that the ring patterns correspond to the diffraction plane of each TMD (002 plane) and AuNPs (JCPDS file: 04-0784).

3.2. Morphology and Structure of TMD/AuNP Electrodes. SEM images of each TMD/AuNPs sample are shown in Figure 3a–c to determine the surface morphology of the electrodes. Note that TMD/AuNP samples were prepared on fresh Si/SiO_2 substrates for SEM imaging (see optical images in Figure S3). The samples were prepared at a comparable amount of AuNPs ($\sim 4.56 \times 10^{11}$ particles) with a constant mass of TMD support (2.13 μg), which was like an electrode on a GCE (30 μg cm^{-2}). It has been demonstrated that most TMD nanosheets were generally stacked horizontally on each other like a laminar structure; see enlarged SEM images in Figure 3a–c, bottom.[6,31,32] This pattern is more pronounced for the MoS_2/AuNPs due to a great perfect

https://doi.org/10.1021/acs.inorgchem.4c02668
Inorg. Chem. 2024, 63, 18750−18762

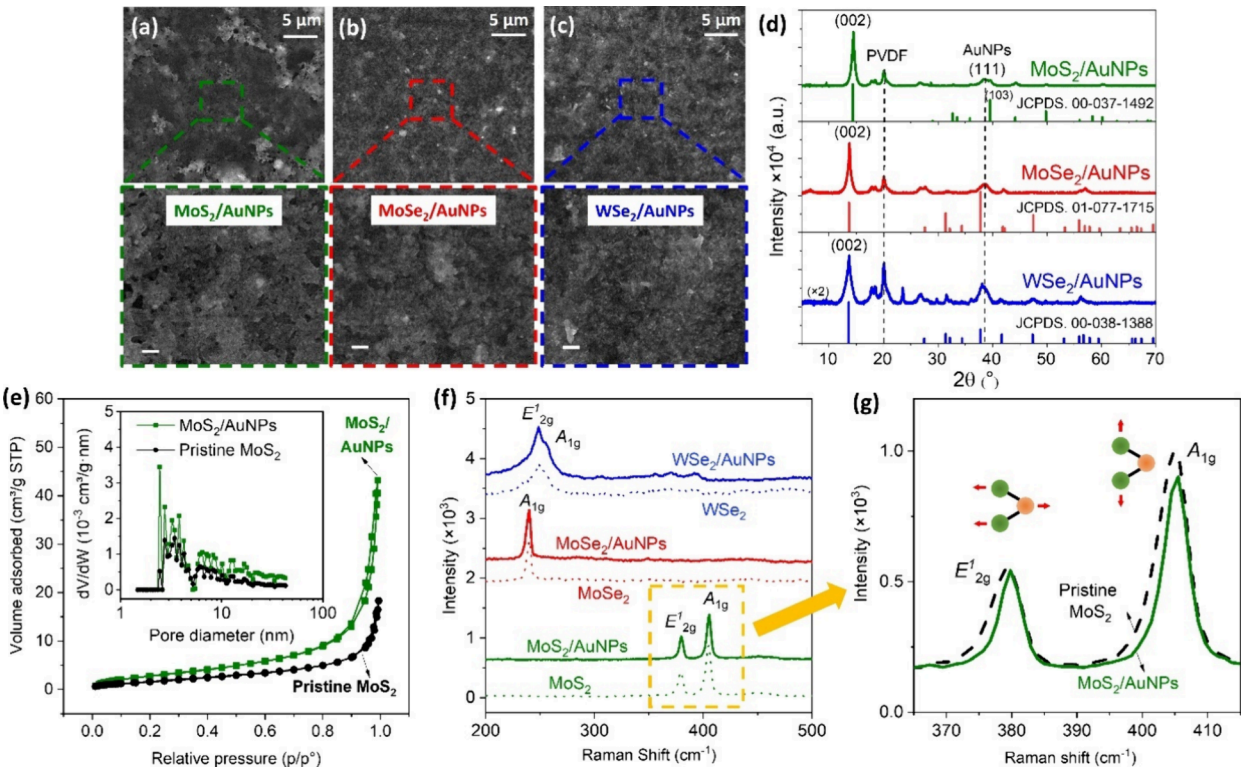

Figure 3. TMD/AuNPs electrodes. SEM images of (a) MoS_2/AuNPs, (b) $MoSe_2$/AuNPs, and (c) WSe_2/AuNPs with their enlarged SEM images (bottom). Note that all scale bars are 500 nm. (d) The PXRD pattern of all TMD/AuNPs showing the characteristic peaks of (002) for TMD and (111) for AuNPs, comparing to corresponding reference patterns of MoS_2 (JCPDS. 00-037-1492), $MoSe_2$ (JCPDS. 01-077-1715), and WSe_2 (JCPDS. 00-038-1388). (e) N_2 adsorption−desorption isotherms of MoS_2/AuNPs and pristine MoS_2 with their corresponding pore-size distributions. (f) Raman spectra of each TMD/AuNPs (solid line) compared to its pristine one (dash line). (g) Enlarged Raman spectra of the MoS_2/AuNPs. Note all TMD/AuNPs samples were prepared at a comparable amount of AuNPs of ~4.56×10^{11} particles with a constant TMD mass of 2.13 μg.

laminar structure of the stacked MoS_2 sheets, while the others exhibit randomly stacked nanosheets during electrode formation. In addition, the TMD/AuNPs samples were also determined using energy dispersive spectroscopy (EDS) showing elemental mapping of the TMD/AuNPs (Figure S4). It was shown that the Au element (red spots) is well-dispersed and homogeneously distributed throughout the electrode surface.

To further investigate electrode compositions, each TMD/AuNPs sample was prepared on a PVDF filter, as shown in Figure S5. It is clearly seen that the electrode morphology on PVDF is well-uniformed, suggesting its possible use in real applications. Figure 3d shows the PXRD patterns of all TMD/AuNPs exhibiting the characteristic (111) peak of AuNPs and the (002) peak of each TMD support. All PXRD patterns were corrected using the referencing PVDF peak of 20.17°.[6] Note that all TMD/AuNPs were prepared at a comparable amount of AuNPs with a constant TMD mass loading. Moreover, the thickness of TMD/AuNP samples on PVDF filters was also measured to estimate the electrode density (see Figure S5). It was found that the densities of MoS_2/AuNPs, $MoSe_2$/AuNPs, and WSe_2/AuNPs were 1.81, 3.42, and 3.46 g cm^{-3}, respectively. It was observed that the density of the MoS_2/AuNPs electrode is far lower than that of a bulk MoS_2 (5.06 g cm^{-3}),[33] demonstrating highly porous structures of the MoS_2/AuNPs electrode. The porous structure of the as-prepared electrodes can be determined by the nitrogen adsorption−desorption technique. Figure 3e compares the N_2 adsorption of the MoS_2/AuNPs and pristine MoS_2. The average pore volume of the MoS_2/AuNPs was calculated to be 0.0668 cm^3 g^{-1}, which was far higher than that of the pristine one (0.0284 cm^3 g^{-1}). It was clearly seen that the adsorption step associated with capillary condensation of the MoS_2/AuNPs significantly increased to higher pressure, exhibiting an increase in the mesopore size.[34] This is supported by the pore-size distribution, as shown in Figure 3e: inset. The hysteresis loop at higher pressure (P/P_0 = 0.9−0.992) observed only for the MoS_2/AuNPs may result from the interparticle texture between AuNPs and the MoS_2 support. This agrees well with previous literature studying the porous structure of the carbon/MoS_2 heteronanosheets.[35]

Moreover, the structure of the TMD/AuNPs and pristine TMD was analyzed by Raman spectroscopy, as shown in Figure 3f. The main vibrational modes of MoS_2/AuNPs and pristine MoS_2 were assigned for the E^1_{2g}-band (380 cm^{-1}) and A_{1g}-band (405 cm^{-1}).[6] The $MoSe_2$/AuNPs and pristine $MoSe_2$ were assigned for A_{1g}-band (239 cm^{-1}).[36] The E^1_{2g}-band (249 cm^{-1}) and A_{1g}-band (257 cm^{-1}) were assigned to the main band for WSe_2/AuNPs and pristine WSe_2, respectively.[27] The results indicate that the TMD/AuNPs and their pristine consist of similar vibration modes with the splitting values between E^1_{2g} and A_{1g} of the MoS_2 (~25 cm^{-1}) assigned to the multilayer.[37] However, the interaction between AuNPs and the MoS_2 support can stiffen the vibration of the S−Mo−S structure, causing a slightly blue shift of the E_{2g} and A_{1g} bands, as shown in Figure 3g (further discussed in XPS analysis).[38]

To evaluate the amount of Au contents, the TMD/AuNPs and pristine TMDs were also analyzed using X-ray fluorescence

https://doi.org/10.1021/acs.inorgchem.4c02668
Inorg. Chem. 2024, 63, 18750−18762

(XRF), as shown in Figure S6. Tables S2−S4 show the weight percentage of elements for each TMD/AuNP compared with the pristine one. The samples for XRF analysis were prepared on a PVDF filter at a comparable amount of AuNPs with a constant TMD loading, like an electrode preparation on a GCE. The results show that the MoS_2/AuNPs contain a large proportion of the Au element ca. 29%, which is much higher than that of $MoSe_2$/AuNPs (∼14% Au) and WSe_2/AuNPs (∼4% Au). Moreover, we also determined the Au content of the TMD/AuNPs by using EDS analysis (Table S5). The samples were prepared on a Si/SiO_2 substrate. The amount of Au contents for MoS_2/AuNPs, $MoSe_2$/AuNPs, and WSe_2/AuNPs were ∼18, ∼11, and ∼4%, respectively, which agree well with XRF analysis. This clearly indicates that high Au content refers to a large amount of the AuNP decoration on the MoS_2 support, which significantly impacts excellent electrocatalytic HER performance.

To get more supportive data about the structural compositions, which is key to revealing the interaction between AuNPs and TMD support, X-ray photoelectron spectroscopy (XPS) was utilized to analyze the pristine TMDs and TMD/AuNPs, as shown in Figure 4. The XPS fitting was carried out

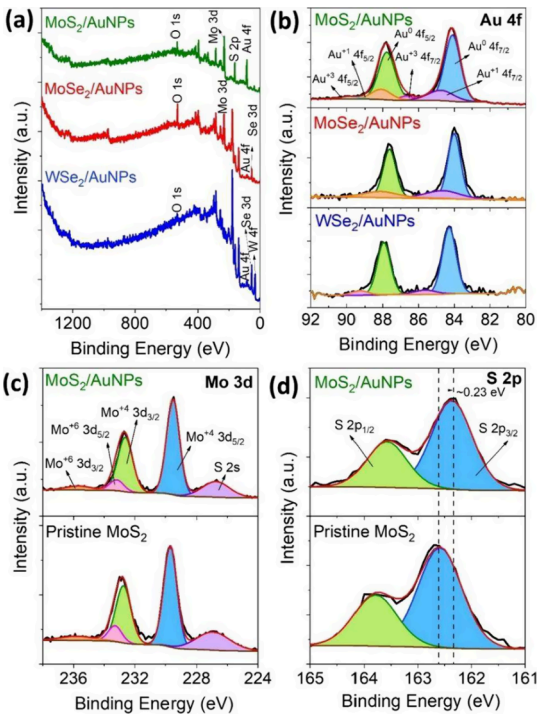

Figure 4. XPS spectra of TMD/AuNPs samples. (a) XPS survey scan of MoS_2/AuNPs, $MoSe_2$/AuNPs, and WSe_2/AuNPs. (b) XPS spectra of Au 4f for each TMD/AuNPs. XPS spectra of (c) the Mo 3d and (d) S 2p peaks of the MoS_2/AuNPs and pristine MoS_2. All XPS spectra were calibrated using C 1s at a binding energy of 284.8 eV.

using CasaXPS with the Kratos library. All XPS spectra were calibrated using C 1s at a binding energy of 284.8 eV. Figure 4a shows the XPS survey of each TMD/AuNPs, showing their corresponding TMD elements with Au. The XPS survey of pristine TMDs is shown in Figure S7. Figure 4b shows XPS spectra of Au^0 4f for each TMD/AuNPs, exhibiting the signal of Au^0 $4f_{7/2}$ (∼84.1 eV) and Au^0 $4f_{5/2}$ (∼87.8 eV).[38,39] As shown within the associated XPS peak fitting results, the partial oxidation of Au on the support was found to be Au(I) and Au(III) which correspond to Au $4f_{7/2}$ oxide states of ∼85.2 and ∼86.3 eV, respectively.[40−42] Figure 4c shows the XPS spectra of Mo 3d of the MoS_2/AuNPs and pristine MoS_2. The Mo 3d spectra are assigned to Mo (+4) and Mo (+6) oxidation states. The presence in the amount of octahedrally coordinated molybdenum atoms (Mo^{6+}) results from the partial oxidation reaction during the exfoliation process.[4,6,43] Moreover, the XPS spectra of Mo 3d and S 2p for the MoS_2/AuNPs and a pristine one were compared, as shown in Figure 4c,d, in which a significant shift to a lower binding energy (∼0.23 eV) is seen after AuNP loading. The shift in binding energy is attributed to a charge transfer from the AuNPs to the MoS_2 support, suggesting a particular interaction at the Au-MoS_2 interface state.[39,44] This interaction was also observed for the $MoSe_2$/AuNPs (Figure S8). The charge transfer process can be explained by the energy level diagram, in which the electron from AuNPs can be transported to the conduction band of the MoS_2 ($MoSe_2$) material. This is because Au and MoS_2 ($MoSe_2$) have a low Schottky barrier, causing an effective electron transport.[38,45] In the case of WSe_2/AuNPs, the charge transfer was not seen due to no shift in the binding energy (Figure S9). This may result from the large Schottky barrier between the WSe_2 and the Au metal, thus enabling an ineffective electron transfer.[46,47]

Based on the charge transfer mechanism, the stronger interaction between Au metals and MoS_2 and $MoSe_2$ supports can emerge under a chemisorption process,[39,44] rather than a normal physisorption process for a WSe_2 support (van der Waals interaction).[47] As a result, the charge transfer at the interface results in the MoS_2/AuNPs more *n*-type, which can facilitate catalytic HER performance, as previously reported in the literature.[38,39] However, we have not observed a shift in the binding energy of gold even when the charge transfer has arisen. This is because the AuNPs surface in the manner used in this study was surrounded by citrate anions, which can compensate for the electron-deficient AuNPs.[48,49] Note that the XPS samples were carried out with the initial catalysts, in which the electrochemical tests have not been performed yet. To further investigate the charge transfer mechanism, the XPS analysis of MoS_2/AuNPs after catalytic activity was also compared, in which the Au 4f binding energy position was significantly shifted *ca.* + 0.6 eV. This corresponds to the charge transfer from the Au metal to MoS_2 support.[38,39] The reason for this point will be discussed in the MoS_2/AuNPs after the catalytic stability test.

3.3. Electrochemical Performance. The electrocatalytic activity of TMD/AuNPs samples is shown in Figure 5 for a comparison of the HER performance. Figure 5a shows the polarization curves of all TMD/AuNPs and solely AuNPs at the amount of AuNPs of 4.56×10^{11} particles, compared to each pristine TMD, and Pt. It is clearly seen that the MoS_2/AuNPs exhibit excellent HER performance due to the onset potential being close to Pt. The optimal amount of AuNPs loading is ca. 4.56×10^{11} particles at a constant TMD support of 2.13 μg (equivalent to 30 $\mu g\ cm^{-2}$). It was found that the overpotential at 10 mA cm^{-2} of MoS_2/AuNPs (−0.21 V) is much lower than that of $MoSe_2$/AuNPs (−0.53 V) and WSe_2/AuNPs (−0.46 V). This is due to well-dispersed AuNPs on MoS_2 support (discussed in TEM images) with a great amount of Au contents on MoS_2/AuNPs (discussed in XRF and EDS analyses) playing a crucial role in enhancing HER performance, indicating the MoS_2 nanosheets behave as an excellent TMD support for decorating AuNPs. Moreover, the over-

https://doi.org/10.1021/acs.inorgchem.4c02668
Inorg. Chem. 2024, 63, 18750−18762

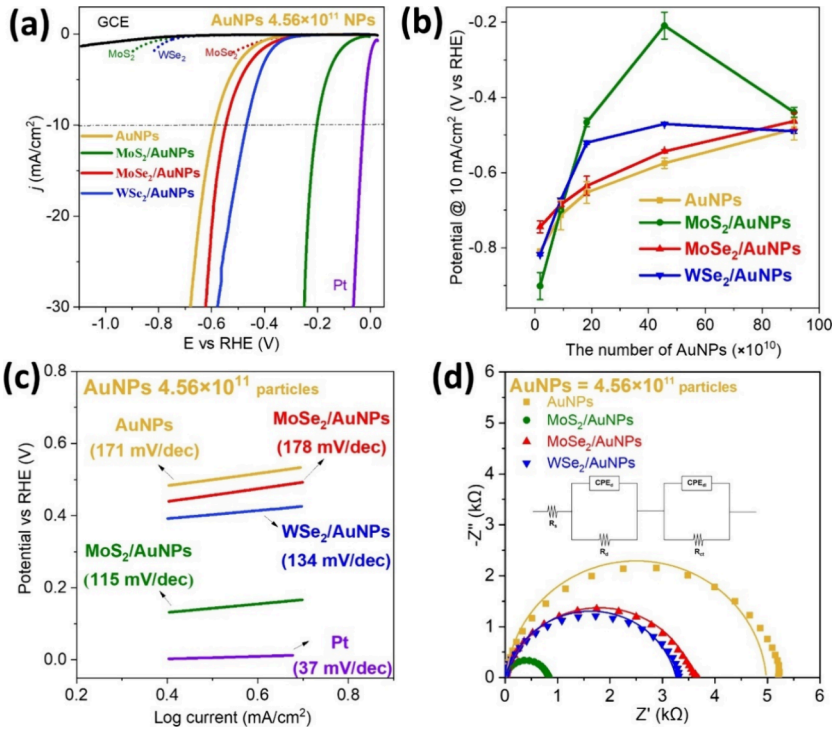

Figure 5. Electrochemical performance. (a) Polarization curves of MoS_2/AuNPs (green line), $MoSe_2$/AuNPs (red line), WSe_2/AuNPs (blue line), and pristine TMDs (color dash line) at the amount of AuNPs of 4.56×10^{11} particles, compared to pristine AuNPs (gold line), Pt, and bare GCE. (b) The overpotentials (vs RHE) plots at 10 mA cm^{-2} of all TMD/AuNPs as various amounts of AuNPs loading. (c) Tafel slopes of all TMD/AuNPs electrodes. (d) Electrochemical impedance spectroscopy (EIS) of all TMDs at an equivalent amount of AuNPs with an applied potential of −0.3 V vs RHE, with its corresponding dual-Randles in series equivalent circuit model.

Table 1. Comparison of the Catalytic Performance of the TMD/AuNPs and Other Au-containing TMD Catalysts for Hydrogen Evolution Reaction

catalyst	onset potential (vs RHE)	overpotential (mV)@ 10 mA cm^{-2}	Tafel slope (mV dec^{-1})	ref
AuNP@MoS_2	∼−220	−323	110	39
Au-5/MoS_2	∼−170	−236	92	25
Au−MoS_2-100	−120	∼−210	163	50
Au-MoS_2	−220	∼−330	86	38
2H-MoS_2@Ag/AuNPs	∼−172	−263	53	51
MoS_2/AuNPs	**−88**	**−209**	**115**	**this work**
$MoSe_2$/AuNPs	**−352**	**−539**	**175**	**this work**
WSe_2/AuNPs	**−350**	**−460**	**134**	**this work**

potentials at 10 mA cm^{-2} of each TMD/AuNPs as a function of AuNPs loading (i.e., $\sim 1.82 \times 10^{10}$ to $\sim 9.12 \times 10^{12}$ particles) are shown in Figure 5b, and their corresponding polarization curves are presented in Figure S10. As a result, the overpotential decreased with an increase in the amount of the AuNP loading for all TMD/AuNP electrodes. In the case of the MoS_2/AuNPs, the overpotential dramatically decreased as a function of AuNPs loading, which is up to $\sim 4.56 \times 10^{11}$ particles of AuNPs, indicating a high active surface area for the HER. This is attributed to a high degree of AuNP distribution on the MoS_2 support as well as the presence of a charge transfer mechanism, giving rise to more *n*-type MoS_2/AuNP characteristics for enhanced HER activity. However, at overloaded AuNPs of $\sim 9.12 \times 10^{12}$ particles, the inverse of overpotential is observed, and its performance is equivalent to pure AuNPs (without TMD support). This is attributed to the agglomeration of AuNPs on the TMD support, leading to a decrease in the active surface area. This agrees well with our previous work studying size-dependent graphene as the AuNP support.[31]

To investigate the kinetic activity of the TMD/AuNPs, Tafel slopes are shown in Figure 5c. It can be clearly seen that the Tafel slope of MoS_2/AuNPs (115 mV dec^{-1}) is much lower than that of $MoSe_2$/AuNPs (175 mV dec^{-1}), WSe_2/AuNPs (134 mV dec^{-1}), and pristine AuNPs (177 mV dec^{-1}) at a comparable amount of AuNP loading ($\sim 4.56 \times 10^{11}$ particles). This indicates that the HER kinetic activity of the MoS_2/AuNPs relates to the Volmer−Heyrovsky mechanism due to the slope being less than 120 mV dec^{-1}, suggesting rapid electron transfer kinetics.[31,52] The Tafel analysis of all TMD/AuNPs as a function of the amount of AuNP loading is presented in Figure S11. In addition, electrochemical performances of the TMD/AuNPs and other Au-containing MoS_2 electrocatalysts are compared in Table 1. It is clearly seen that the onset potential of as-prepared MoS_2/AuNPs (88 mV) is far lower than that of previously reported Au-supported MoS_2, such as Galvanic deposition of AuNP on MoS_2 (AuNP@MoS_2,

https://doi.org/10.1021/acs.inorgchem.4c02668
Inorg. Chem. 2024, 63, 18750−18762

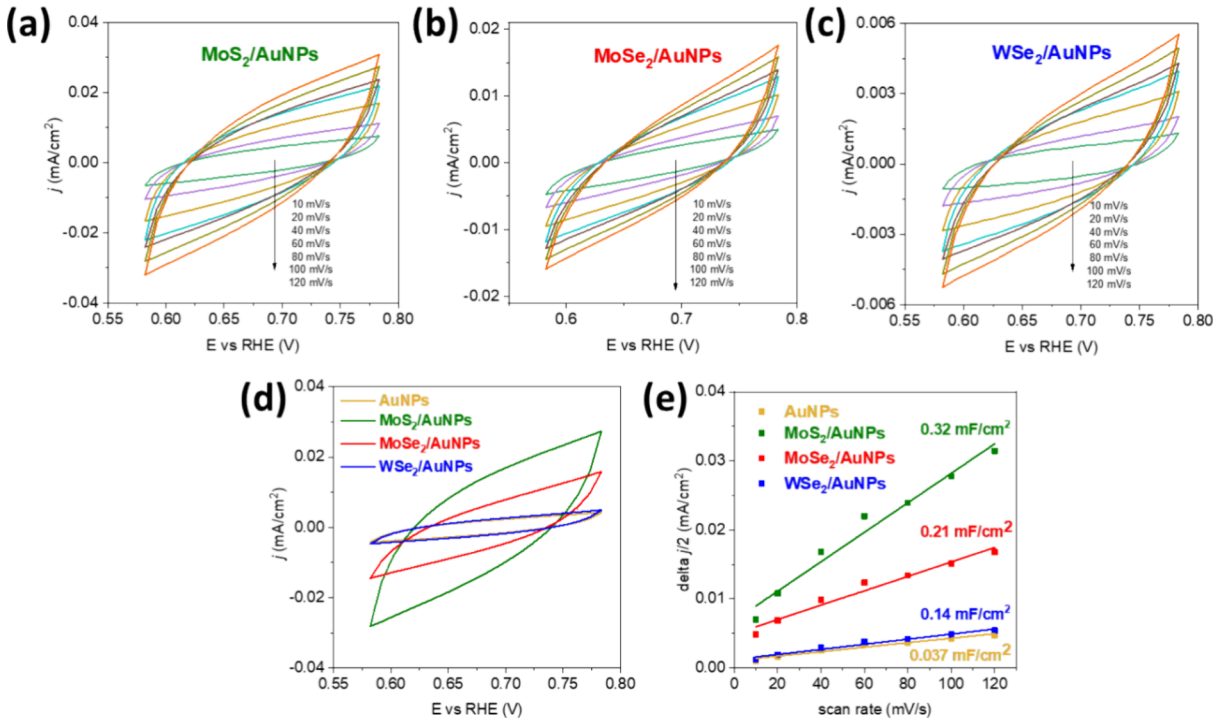

Figure 6. Cyclic voltammetry (CV) analysis of (a) MoS_2/AuNPs, (b) $MoSe_2$/AuNPs, and (c) WSe_2/AuNPs at a nonfaradaic potential window between 0.55 and 0.75 V (vs RHE). (d) CV curve comparison of each TMD/AuNPs and pristine AuNPs at a scan rate of 10 mV s^{-1}. (e) Linear plots of the capacitive current density of $\Delta J/2$ versus the scan rates for TMD/AuNPs and pristine AuNPs. ΔJ is the difference in the anodic and cathodic current densities ($\Delta J = J_{anodic} - J_{cathodic}$). The slopes of linear plots are the areal capacitance (area of glassy carbon electrode). Note that all electrodes were prepared at a comparable amount of AuNPs loading of 4.56×10^{11} particles for 2.13 μg of TMD as a support (equivalent to 30 μg cm^{-2}).

−220 mV),[39] pulsed laser deposition of Au on MoS_2 (Au-5/MoS_2, −170 mV),[25] in situ grown AuNPs on MoS_2 (Au−MoS_2-100, −120 mV),[50] Au nanorods on MoS_2 (Au-MoS_2, −220 mV),[38] as well as Ag/Au nanocomposites on MoS_2 (2H-MoS_2@Ag/AuNPs, −160 mV).[51] Moreover, the overpotential at 10 mA cm^{-2} of electrocatalysts was also compared in Table 1, indicating that as-prepared MoS_2/AuNPs possess a low overpotential for HER performance (close to Pt one). In terms of kinetic activity, the Tafel slope of MoS_2/AuNPs (115 mV dec^{-1}) exhibits good electrocatalytic activity which is in the range of other Au-containing electrocatalysts as previously reported (86−163 mV dec^{-1}).[25,38,39,50,51] In addition, due to the instability of WS_2 nanosheets in a mixture of isopropanol and water (Figure S12 in the Supporting Information), thus WS_2 dispersion was prepared using acetonitrile as a solvent for comparison. The HER performances of WS_2/AuNPs and pristine WS_2 are presented in Figure S13. It was found that the catalytic activity of WS_2/AuNPs (155 mV/dec) is still far lower than that of MoS_2/AuNPs (115 mV/dec) at a comparable amount of AuNPs loading.

In addition, electrochemical impedance spectroscopy (EIS) analysis was used to determine the conductivities and electrocatalytic kinetics of the as-prepared electrodes. Figure 5d shows the Nyquist plots of TMD/AuNPs and the sole AuNPs electrodes at a comparable amount of AuNPs of 4.56×10^{11} particles. All electrodes were applied with a constant potential of −0.3 V (vs RHE). Based on typical EIS analysis, solution resistance (R_s) and charge transfer resistance (R_{ct}) can be directly obtained from the Nyquist plots.[31,39] The R_s, the bulk solution resistance, can be obtained from the intercept of the initial point of the semicircle. R_{ct}, the active material resistance, can be calculated by the diameter of the semicircle. In general, the R_{ct} value relates to high electrochemical activity and conductivity. As shown in Figure 5d, the R_{ct} of MoS_2/AuNPs (~0.84 kΩ) is much lower than that of WSe_2/AuNPs (~3.30 kΩ), $MoSe_2$/AuNPs (~3.64 kΩ), and pristine AuNPs (~5.20 kΩ), indicating high electrode conductivity and a fast kinetic reaction for MoS_2 as an AuNP support. The inset in Figure 5d shows a dual-Randles in a series equivalent circuit model, which agrees well with the previous literature.[39] It was found that the first RC branch (i.e., R_dCPE_d) corresponds to the electrode geometry or the diffusion barrier from the hydrogen evolution, which is not relevant to the kinetic reaction. The second RC branch (i.e., $R_{ct}CPE_{dl}$) can refer to the kinetic activities for the HER, in which R_{ct} and C_{dl} correspond to the reaction kinetics and the electrochemical surface area (ECSA) of the electrodes, respectively.[31,39,53] The corresponding R_s and R_{ct} for TMD/AuNPs at different AuNPs loadings are presented in Table S6. Among those electrocatalytic results (i.e., the low overpotential, low Tafel slopes, and low R_{ct} values), it apparently indicates that the MoS_2/AuNPs exhibit excellent electrochemical performance for HER activity. The EIS spectra of the TMD/AuNPs electrodes at different amounts of AuNPs loading are also presented in Figure S14.

To gain insight into the electrocatalytic performance of as-prepared electrodes, TMD/AuNPs and pristine AuNPs electrodes at a comparable amount of AuNPs loading (4.56×10^{11} particles) were evaluated using cyclic voltammetry (CV), as shown in Figure 6a−c. The CV was performed at a nonfaradaic reaction during a potential window of 0.55−0.75 V (vs RHE) as a function of scan rates (10−120 mV s^{-1}). Figure

https://doi.org/10.1021/acs.inorgchem.4c02668
Inorg. Chem. 2024, 63, 18750−18762

6d shows a comparison of the CV of each electrode at 10 mV s^{-1}. It is worth noting that the MoS_2/AuNPs have a larger current density than that of others. For quantitative analysis, the areal capacitances of each TMD/AuNPs can be obtained from the slope of the current density against scan rates. The areal capacitances of MoS_2/AuNPs, $MoSe_2$/AuNPs, WSe_2/AuNPs, and pristine AuNPs correspond to 0.32, 0.21, 0.14, and 0.037 mF cm^{-2} (Figure 6e). This indicates that the excellent TMD support (i.e., MoS_2/AuNPs) possesses a high double layer capacitance (C_{dl}) which is estimated at almost 1 order of magnitude compared to solely AuNPs, demonstrating greater electrochemically active surface area.

To obtain more supportive data, each TMD/AuNP was also analyzed using the gravimetric capacitance (i.e., specific capacitance) as a function of scan rates (1−200 mV s^{-1}), as shown in Figure 7a. The total mass of the as-prepared

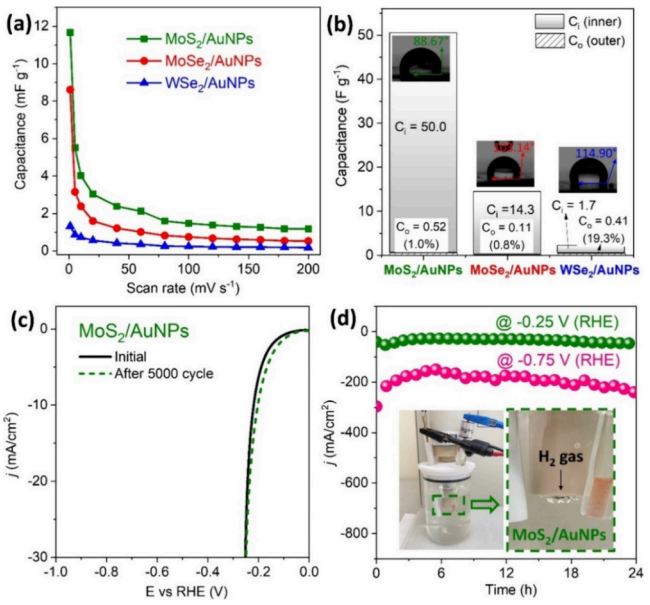

Figure 7. Dependent scan rates. (a) Gravimetric capacitance of TMD/AuNPs at various scan rates of 1−200 mV s^{-1}. The total mass of each electrode (~2.70 μg) can be estimated from a combination of the TMD mass (~2.13 μg) and AuNPs loading (~0.574 μg) on a GCE. (b) Total capacitance (C_{total}; assuming at very low scan rate) consists of the outer capacitance (C_o; assuming at very high scan rate) and the inner capacitance ($C_i = C_{total} - C_o$). Insets show photographs of water contact angle of each TMD/AuNP electrode at 60 s after dropping water droplet. (c, d) Stability tests. (c) Polarization curves of the MoS_2/AuNPs electrode before and after applied 5000 cycles of the potentials window 0.1−0.3 V vs RHE with the scan rate of 100 mV s^{-1}. (d) Chronoamperometry of the MoS_2/AuNPs applied at −0.25 and −0.75 V (vs RHE) for 24 h. The measurement was performed in a three-electrode system under 0.5 M H_2SO_4, which uses a glassy carbon rotating disk electrode (RDE), carbon rod, and Hg/Hg_2Cl_2 as a working electrode, counter electrode, and reference electrode, respectively. Inset in (d) shows the experimental setup.

electrodes (~2.70 μg) was calculated by the summation of the mass of the TMD support (~2.13 μg) and AuNPs loading (~0.574 μg) on a GCE. It is worth noting that the gravimetric capacitance of MoS_2/AuNPs is greater than that of other electrodes at a comparable AuNPs loading (4.56×10^{11} particles), which is in accordance with areal capacitance in Figure 6e. This indicates the high electrochemical surface area for the MoS_2/AuNPs electrode, implying a large number of exposed active sites of AuNPs on the MoS_2 support for HER activity.

In addition, we also used Trasatti's method to further analyze the origin of different capacitive charge storage of each TMD/AuNPs.[54,55] This method is used to consider the capacitance arising from an external surface charge storage, so-called the outer capacitance (C_{outer}), and internal and deep surface layer charge storage, so-called the inner surface capacitance (C_i). The outer capacitance (C_o) is estimated when the scan rate is close to infinity ($\upsilon \rightarrow \infty$; a very short period of time that charges can be stored at the outer electrode surface), while the total capacitance (C_{total}) is evaluated when the scan rate is close to zero ($\upsilon \rightarrow 0$; a sufficient time that charges can be stored at outer and inner electrode surfaces, meaning all active surface areas).[31,54,56] Thus, the different capacitance between C_{total} and C_o informs the inner capacitance ($C_i = C_{total} - C_o$). Further analysis of Trasatti's method is described in Figure S15.

According to Trasatti's method giving differential capacitances, Figure 7b shows the C_i and the C_o of TMD/AuNPs electrodes. It is clearly seen that the total capacitance (C_{total}) of MoS_2/AuNPs (~50 F g^{-1}) is far higher than that of $MoSe_2$/AuNPs (~14 F g^{-1}) and WSe_2/AuNPs (~2 F g^{-1}). The major portion of the capacitance of the MoS_2/AuNPs electrode arises mostly from the C_i which is estimated to be 99% of the C_{total}, indicating a high electrochemical surface area. This is attributed to the high wettability of the MoS_2/AuNPs surface possessing a water contact angle (WCA) of ~89° (see insets in Figure 7b), which is much lower than that of $MoSe_2$/AuNPs (~103°) and WSe_2/AuNPs (~115°). Further WCA analysis is presented in Figure S16. The high hydrophilic property of MoS_2/AuNPs results from the perfect laminar stacked MoS_2 nanosheets with a low electrode density (see the SEM cross-section in Figure S5), giving the highly porous electrode. This can allow the flow of ionic electrolytes to infiltrate the deep pore or deep surface area of the electrode, which plays an important role in increasing ECSA for enhanced HER activity.

The long-term stability of the as-prepared electrocatalysts is one of the important factors in the real-world HER process. We performed the stability test using two techniques: polarization curve after 5000 cycles and chronoamperometry for over 24 h. The stability tests of the MoS_2/AuNP electrode were carried out after sweep potentials for 5000 cycles with the potentials window of 0.1−0.3 V vs RHE at a scan rate of 100 mV s^{-1} under an acidic electrolyte. It was found that the polarization curve of the MoS_2/AuNPs after cycles exhibited no significant change when compared to the initial one, demonstrating the high durability of the as-prepared catalyst (Figure 7c). Furthermore, the stability of MoS_2/AuNPs was also determined using time-dependent stability, which was performed at a constant overpotential of −0.25 and −0.75 V vs RHE over 24 h (Figure 7d). The setup was performed under nitrogen purging using a glassy carbon rotating disk electrode (RDE) as the working electrode at a rotation of 2500 rpm. The inset in Figure 7d shows the experiment with the formation of hydrogen gas at the electrode. The results showed that the current density can be maintained around −35 mA cm^{-2}, confirming an effective HER performance of the MoS_2/AuNPs. To mimic the use of the catalyst in real-world applications, the MoS_2/AuNPs were also tested under ultrahigh current density at 200 mA cm^{-2} (Figure 7d). It is clearly seen that the catalyst can still perform excellent hydrogen production for over 24 h.

https://doi.org/10.1021/acs.inorgchem.4c02668
Inorg. Chem. 2024, 63, 18750−18762

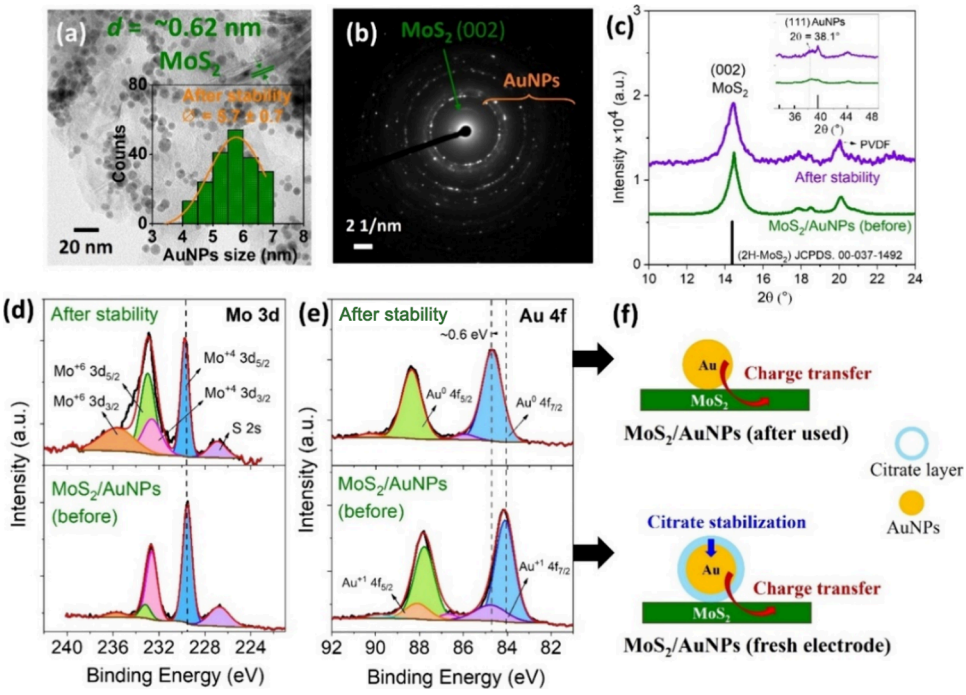

Figure 8. MoS_2/AuNPs after catalytic stability test. (a) TEM image of MoS_2/AuNPs with the size distribution of AuNPs and (b) corresponding SAED image. (c) PXRD pattern of MoS_2/AuNPs before and after use. Comparing XPS spectra of (d) Mo 3d and (e) Au 4f. (f) Schematic showing the charge transfer from gold to MoS_2 in the presence (initial catalyst) and absence (after use) of citrate anions as a stabilizer.

To determine the physical and electronic properties of MoS_2/AuNPs after the catalytic stability test, TEM, PXRD, and XPS were performed as shown in Figure 8. It was found that the AuNPs were well-uniformed and still deposited on the support, and their variability in size was around 4−7 nm with a mean particle size of 5.7 nm (Figure 8a). This indicated that there was no significant change in the size distribution of AuNPs after catalytic activities. The SAED and PXRD techniques were carried out to investigate the change in the crystal structure (Figure 8b,c). It was found that the diffraction patterns of MoS_2 and AuNPs did not alter when compared with the initial ones. Moreover, we also performed XPS analysis to determine the change in chemical and electronic states of the Mo and Au atoms. Figure 8d shows an increase in the intensity of oxide peaks (Mo^{6+}) for the catalyst after use, which may result from oxidation on the MoS_2 surface during HER activities. The presence of the oxide form in the MoS_2/AuNPs structure can also facilitate the HER activity, as previously reported in the literature.[57] Interestingly, it is clearly seen that the XPS spectra of Au for the catalyst after use was shifted +0.6 eV when compared to the initial catalyst (Figure 8e), sole AuNPs, and Au foil possessing a binding energy of 84 eV.[39,48] This indicated the shift to the higher binding energy of Au (after catalytic activity) which results from the charge transfer from Au to the MoS_2 support causing electron-deficient Au (Figure 8f).[38,39] In this case, the citrate anions attached to the gold surface can be released somehow during the HER activities. However, in the case of the initial catalyst, the change in binding energy was not observed even when the charge transfer from the Au metal to the MoS_2 support arose (aforementioned in XPS analysis). This is due to the charge stabilization from the negatively charged citrate anions surrounding the AuNP surface.[48,49]

4. CONCLUSIONS

In conclusion, we have determined the electrochemical and physical performances of two-dimensional transition metal dichalcogenide nanosheets (MoS_2, $MoSe_2$, and WSe_2) as AuNP supports (TMD/AuNPs). The MoS_2 nanosheets, as a support for decorating AuNPs (MoS_2/AuNPs), exhibit outstanding electrocatalytic for HER activity, compared to the $MoSe_2$/AuNPs and WSe_2/AuNPs, as well as previously reported Au-containing TMD electrocatalysts. The MoS_2/AuNPs at the optimal proportion of the AuNP loading exhibit excellent HER performance due to an abundance of exposed active sites (well-dispersed AuNPs on MoS_2 support), highly electrochemical surface area (greater areal and specific capacitances), high wettability, as well as high electrode conductivity (low R_{ct}). The charge transfer from AuNPs to the MoS_2 support can also increase the *n*-type semiconductor, which can assist catalytic HER performance. Moreover, the MoS_2/AuNPs exhibit excellent long-term stabilities after 5000 cycles and ultrahigh current density (~200 mA cm^{-2}) for over 24 h. Therefore, our study demonstrated insights into the role of TMD as a support for decorating nanoparticles, which could have the potential to develop a future TMD-based catalyst for real-world HER applications.

■ ASSOCIATED CONTENT

Supporting Information

The Supporting Information is available free of charge at https://pubs.acs.org/doi/10.1021/acs.inorgchem.4c02668.

Further sample characterization including DLS, SEM, TEM, EDX, XRF, XPS, water contact angle analysis, and further electrochemical measurement results and analysis (PDF)

https://doi.org/10.1021/acs.inorgchem.4c02668
Inorg. Chem. 2024, 63, 18750−18762

AUTHOR INFORMATION

Corresponding Author

Wisit Hirunpinyopas − *Department of Chemistry, Faculty of Science, Kasetsart University, Bangkok 10900, Thailand;* orcid.org/0000-0002-6147-570X; Email: wisit.hi@ku.ac.th

Authors

Boontarika Saeloo − *Department of Chemistry, Faculty of Science, Kasetsart University, Bangkok 10900, Thailand*

Thanit Saisopa − *Department of Applied Physics, Faculty of Sciences and Liberal Arts, Rajamangala University of Technology Isan, Nakhon Ratchasima 30000, Thailand*

Panwad Chavalekvirat − *School of Bio-Chemical Engineering and Technology, Sirindhron International Institute of Technology and Research Unit in Sustainable Electrochemical Intelligent, Thammasat University, Pathum Thani 12120, Thailand*

Pawin Iamprasertkun − *School of Bio-Chemical Engineering and Technology, Sirindhron International Institute of Technology and Research Unit in Sustainable Electrochemical Intelligent, Thammasat University, Pathum Thani 12120, Thailand;* orcid.org/0000-0001-8950-3330

Kulpavee Jitapunkul − *Department of Chemical Engineering, Faculty of Engineering, Kasetsart University, Bangkok 10900, Thailand*

Weekit Sirisaksoontorn − *Department of Chemistry, Faculty of Science, Kasetsart University, Bangkok 10900, Thailand;* orcid.org/0000-0001-6902-4519

T. Randall Lee − *Department of Chemistry and the Texas Center for Superconductivity, University of Houston, Houston, Texas 77204-5003, United States;* orcid.org/0000-0001-9584-8861

Complete contact information is available at: https://pubs.acs.org/10.1021/acs.inorgchem.4c02668

Notes

The authors declare no competing financial interest.

ACKNOWLEDGMENTS

This research has received funding support from the NSRF via the Program Management Unit for Human Resources & Institutional Development, Research and Innovation (grant number B39G670019). B.S. wishes to acknowledge the Development and Promotion of Science and Technology Talents Project (DPST). W.H. wishes to acknowledge funding from Kasetsart University Research and Development Institute, KURDI [grant number FF(KU-SRIU)3.67]. The work at the University of Houston was supported by the Robert A. Welch Foundation (Grant Nos. E-1320 and V-E-0001).

REFERENCES

(1) Tan, C.; Cao, X.; Wu, X. J.; He, Q.; Yang, J.; Zhang, X.; Chen, J.; Zhao, W.; Han, S.; Nam, G. H.; et al. Recent Advances in Ultrathin Two-Dimensional Nanomaterials. *Chem. Rev.* **2017**, *117* (9), 6225−6331.

(2) Chowdhury, T.; Sadler, E. C.; Kempa, T. J. Progress and Prospects in Transition-Metal Dichalcogenide Research Beyond 2D. *Chem. Rev.* **2020**, *120* (22), 12563−12591.

(3) Duan, X.; Wang, C.; Pan, A.; Yu, R.; Duan, X. Two-Dimensional Transition Metal Dichalcogenides as Atomically thin Semiconductors: Opportunities and Challenges. *Chem. Soc. Rev.* **2015**, *44* (24), 8859−8876.

(4) Nualchimplee, C.; Jitapunkul, K.; Deerattrakul, V.; Thaweechai, T.; Sirisaksoontorn, W.; Hirunpinyopas, W.; Iamprasertkun, P. Auto-Oxidation of Exfoliated MoS_2 in N-Methyl-2-Pyrrolidone: From 2D Nanosheets to 3D Nanorods. *New J. Chem.* **2022**, *46* (2), 747−755.

(5) Iamprasertkun, P.; Hirunpinyopas, W.; Deerattrakul, V.; Sawangphruk, M.; Nualchimplee, C. Controlling the flake size of bifunctional 2D WSe_2 nanosheets as flexible binders and supercapacitor materials. *Nanoscale Adv.* **2021**, *3* (3), 653−660.

(6) Hirunpinyopas, W.; Prestat, E.; Worrall, S. D.; Haigh, S. J.; Dryfe, R. A. W.; Bissett, M. A. Desalination and Nanofiltration through Functionalized Laminar MoS_2 Membranes. *ACS Nano* **2017**, *11* (11), 11082−11090.

(7) Hirunpinyopas, W.; Prestat, E.; Iamprasertkun, P.; Bissett, M. A.; Dryfe, R. A. W. Potential Dependent Ionic Sieving Through Functionalized Laminar MoS_2 Membranes. *2D Mater.* **2020**, *7* (1), No. 015030.

(8) Hirunpinyopas, W.; Rodgers, A. N. J.; Worrall, S. D.; Bissett, M. A.; Dryfe, R. A. W. Hydrogen Evolution at Liquid|Liquid Interfaces Catalyzed by 2D Materials. *ChemNanoMat* **2017**, *3* (6), 428−435.

(9) Saisopa, T.; Jitapunkul, K.; Bunpheng, A.; Nakajima, H.; Supruangnet, R.; Busayaporn, W.; Sukprom, T.; Hirunpinyopas, W.; Seubsai, A.; Songsiriritthigul, P.; et al. The Structure Analysis and Chemical Properties Probing During Recycling Processes of Transition Metal Dichalcogenides Exfoliation. *Electrochim. Acta* **2023**, *449*, No. 142171.

(10) Bar-Ziv, R.; Ranjan, P.; Lavie, A.; Jain, A.; Garai, S.; Bar Hen, A.; Popovitz-Biro, R.; Tenne, R.; Arenal, R.; Ramasubramaniam, A.; et al. Au-MoS_2 Hybrids as Hydrogen Evolution Electrocatalysts. *ACS Appl. Energy Mater.* **2019**, *2* (8), 6043−6050.

(11) Razavi, M.; Sookhakian, M.; Goh, B. T.; Bahron, H.; Mahmoud, E.; Alias, Y. Molybdenum Disulfide Nanosheets Decorated with Platinum Nanoparticle as a High Active Electrocatalyst in Hydrogen Evolution Reaction. *Nanoscale Res. Lett.* **2022**, *17* (1), 9.

(12) Fereja, S. L.; Li, P.; Guo, J.; Fang, Z.; Zhang, Z.; Zhuang, Z.; Zhang, X.; Liu, K.; Chen, W. W-Doped MoP Nanospheres as Electrocatalysts for pH-Universal Hydrogen Evolution Reaction. *ACS Appl. Nano Mater.* **2021**, *4* (6), 5992−6001.

(13) Jung, H. y.; Chae, M. J.; Park, J. H.; Song, Y. I.; Ro, J. C.; Suh, S. J. Effects of Platinum Group Metals on MoS_2 Nanosheets for a High-Performance Hydrogen Evolution Reaction Catalyst. *ACS Appl. Energy Mater.* **2021**, *4* (10), 10748−10755.

(14) Sharma, M. D.; Mahala, C.; Basu, M. Nanosheets of $MoSe_2$@M (M = Pd and Rh) Function as Widespread pH Tolerable Hydrogen Evolution Catalyst. *J. Colloid Interface Sci.* **2019**, *534*, 131−141.

(15) Yuan, N.; Jiang, Q.; Wu, Z.; Tang, J. Ru Nanoparticles Decorated on 2D MoO_2 Nanosheets as Efficient and Durable Electrocatalysts for the Hydrogen Evolution Reaction in a Wide pH Range. *J. Phys. Chem. C* **2020**, *124* (20), 10804−10814.

(16) Zhu, J.; Yang, R.; Zhang, G. Atomically Thin Transition Metal Dichalcogenides for the Hydrogen Evolution Reaction. *ChemPhysMater.* **2022**, *1* (2), 102−111.

(17) Yang, J.; Mohmad, A. R.; Wang, Y.; Fullon, R.; Song, X.; Zhao, F.; Bozkurt, I.; Augustin, M.; Santos, E. J. G.; Shin, H. S.; et al. Ultrahigh-Current-Density Niobium Disulfide Catalysts for Hydrogen Evolution. *Nat. Mater.* **2019**, *18* (12), 1309−1314.

(18) Choi, S.; Kwon, K. C.; Kim, S. Y.; Jang, H. W. Tailoring Catalytic Activities of Transition Metal Disulfides for Water Splitting. *FlatChem.* **2017**, *4*, 68−80.

(19) Cheng, N.; Stambula, S.; Wang, D.; Banis, M. N.; Liu, J.; Riese, A.; Xiao, B.; Li, R.; Sham, T. K.; Liu, L. M.; et al. Platinum Single-Atom and Cluster Catalysis of the Hydrogen Evolution Reaction. *Nat. Commun.* **2016**, *7*, 13638.

(20) Ďurovič, M.; Hnát, J.; Bouzek, K. Electrocatalysts for the Hydrogen Evolution Reaction in Alkaline and Neutral Media. A Comparative Review. *J. Power Sources* **2021**, *493*, No. 229708.

(21) Mondal, A.; Vomiero, A. 2D Transition Metal Dichalcogenides-Based Electrocatalysts for Hydrogen Evolution Reaction. *Adv. Funct. Mater.* **2022**, *32* (52), No. 2208994.
(22) Er, D.; Ye, H.; Frey, N. C.; Kumar, H.; Lou, J.; Shenoy, V. B. Prediction of Enhanced Catalytic Activity for Hydrogen Evolution Reaction in Janus Transition Metal Dichalcogenides. *Nano Lett.* **2018**, *18* (6), 3943−3949.
(23) Voiry, D.; Yang, J.; Chhowalla, M. Recent Strategies for Improving the Catalytic Activity of 2D TMD Nanosheets Toward the Hydrogen Evolution Reaction. *Adv. Mater.* **2016**, *28* (29), 6197−6206.
(24) Li, C.; Zhu, L.; Li, H.; Li, H.; Wu, Z.; Liang, C.; Zhu, X.; Sun, Y. Dual Surfactants Applied in Synthesis of $MoSe_2$ for High-Efficiency Hydrogen Evolution Reaction. *J. Alloys Compd.* **2021**, *863*, No. 158092.
(25) Jing, Y.; Wang, R.; Wang, Q.; Wang, X. Gold Nanoclusters Grown on MoS_2 Nanosheets by Pulsed Laser Deposition: An Enhanced Hydrogen Evolution Reaction. *Molecules* **2021**, *26* (24), 7503.
(26) Pataniya, P. M.; Patel, V.; Sumesh, C. K. Electrophoretic Deposition of $MoSe_2$−MoO_x Nanosheets for Enhanced Electrocatalytic Hydrogen Evolution Reaction. *ACS Appl. Energy Mater.* **2021**, *4* (8), 7891−7899.
(27) Muska, M.; Yang, J.; Sun, Y.; Wang, J.; Wang, Y.; Yang, Q. $CoSe_2$ Nanoparticles Dispersed in WSe_2 Nanosheets for Efficient Electrocatalysis and Supercapacitance Applications. *ACS Appl. Nano Mater.* **2021**, *4* (6), 5796−5807.
(28) Rapoport, L.; Fleischer, N.; Tenne, R. Applications of WS_2(MoS_2) Inorganic Nanotubes and Fullerene-like Nanoparticles for Solid Lubrication and for Structural Nanocomposites. *J. Mater. Chem.* **2005**, *15* (18), 1782.
(29) Zhao, Y.; Yang, C.; Mao, G.; Su, J.; Cheng, G.; Luo, W. Ultrafine Rh Nanoparticle Decorated $MoSe_2$ Nanoflowers for Efficient Alkaline Hydrogen Evolution Reaction. *Inorg. Chem. Front.* **2018**, *5* (11), 2978−2984.
(30) Chavalekvirat, P.; Hirunpinyopas, W.; Deshsorn, K.; Jitapunkul, K.; Iamprasertkun, P. Liquid Phase Exfoliation of 2D Materials and Its Electrochemical Applications in the Data-Driven Future. *Precis. Chem.* **2024**, *2* (7), 300−329.
(31) Saeloo, B.; Jitapunkul, K.; Iamprasertkun, P.; Panomsuwan, G.; Sirisaksoontorn, W.; Sooknoi, T.; Hirunpinyopas, W. Size-Dependent Graphene Support for Decorating Gold Nanoparticles as a Catalyst for Hydrogen Evolution Reaction with Machine Learning-Assisted Prediction. *ACS Appl. Mater. Interfaces* **2023**.
(32) Paechotrattanakul, P.; Jitapunkul, K.; Iamprasertkun, P.; Srinoi, P.; Sirisaksoontorn, W.; Hirunpinyopas, W. Ultrahigh Stable Laminar Graphene Membranes for Effective Ionic and Molecular Nanofiltration with a Machine Learning-Assisted Study. *Nanoscale* **2023**, *15* (19), 8716−8729.
(33) Haynes, W. M., Ed.; *CRC Handbook of Chemistry and Physics*; CRC Press, 2011.
(34) Thommes, M.; Kaneko, K.; Neimark, A. V.; Olivier, J. P.; Rodriguez-Reinoso, F.; Rouquerol, J.; Sing, K. S. W. Physisorption of Gases, with Special Reference to the Evaluation of Surface Area and Pore Size Distribution (IUPAC Technical Report). *Pure Appl. Chem.* **2015**, *87* (9−10), 1051−1069.
(35) Fang, Y.; Lv, Y.; Gong, F.; Elzatahry, A. A.; Zheng, G.; Zhao, D. Synthesis of 2D-Mesoporous-Carbon/MoS_2 Heterostructures with Well-Defined Interfaces for High-Performance Lithium-Ion Batteries. *Adv. Mater.* **2016**, *28* (42), 9385−9390.
(36) Balasingam, S. K.; Lee, J. S.; Jun, Y. Few-Layered $MoSe_2$ Nanosheets as an Advanced Electrode Material for Supercapacitors. *Dalton Trans* **2015**, *44* (35), 15491−15498.
(37) Luo, R.; Xu, W. W.; Zhang, Y.; Wang, Z.; Wang, X.; Gao, Y.; Liu, P.; Chen, M. Van der Waals Interfacial Reconstruction in Monolayer Transition-metal Dichalcogenides and Gold Heterojunctions. *Nat. Commun.* **2020**, *11* (1), 1011.
(38) Shi, Y.; Wang, J.; Wang, C.; Zhai, T. T.; Bao, W. J.; Xu, J. J.; Xia, X. H.; Chen, H. Y. Hot Electron of Au Nanorods Activates the Electrocatalysis of Hydrogen Evolution on MoS_2 Nanosheets. *J. Am. Chem. Soc.* **2015**, *137* (23), 7365−7370.
(39) Higgins, E. P. C.; Papaderakis, A. A.; Byrne, C.; Cai, R.; Elgendy, A.; Haigh, S. J.; Walton, A. S.; Lewis, D. J.; Dryfe, R. A. W. High-Performance Nanostructured MoS_2 Electrodes with Spontaneous Ultralow Gold Loading for Hydrogen Evolution. *J. Phys. Chem. C* **2021**, *125* (38), 20940−20951.
(40) Duan, X.; Tian, X.; Ke, J.; Yin, Y.; Zheng, J.; Chen, J.; Cao, Z.; Xie, Z.; Yuan, Y. Size Controllable Redispersion of Sintered Au Nanoparticles by Using Iodohydrocarbon and Its Implications. *Chem. Sci.* **2016**, *7* (5), 3181−3187.
(41) Klyushin, A. Y.; Rocha, T. C.; Havecker, M.; Knop-Gericke, A.; Schlogl, R. A near ambient pressure XPS study of Au oxidation. *Phys. Chem. Chem. Phys.* **2014**, *16* (17), 7881−7886.
(42) Juodkazis, K.; Juodkazyte, J.; Jasulaitiene, V.; Lukinskas, A.; Sebeka, B. XPS Studies on the Gold Oxide Surface Layer Formation. *Electrochem. Commun.* **2000**, *2* (7), 503−507.
(43) Pagona, G.; Bittencourt, C.; Arenal, R.; Tagmatarchis, N. Exfoliated Semiconducting Pure 2H-MoS_2 and 2H-WS_2 Assisted by Chlorosulfonic Acid. *Chem. Commun.* **2015**, *51* (65), 12950−12953.
(44) Velicky, M.; Rodriguez, A.; Bousa, M.; Krayev, A. V.; Vondracek, M.; Honolka, J.; Ahmadi, M.; Donnelly, G. E.; Huang, F.; Abruna, H. D.; et al. Strain and Charge Doping Fingerprints of the Strong Interaction between Monolayer MoS_2 and Gold. *J. Phys. Chem. Lett.* **2020**, *11* (15), 6112−6118.
(45) Kang, Y.; Najmaei, S.; Liu, Z.; Bao, Y.; Wang, Y.; Zhu, X.; Halas, N. J.; Nordlander, P.; Ajayan, P. M.; Lou, J.; et al. Plasmonic Hot Electron Induced Structural Phase Transition in a MoS_2 Monolayer. *Adv. Mater.* **2014**, *26* (37), 6467−6471.
(46) Chen, C.-H.; Wu, C.-L.; Pu, J.; Chiu, M.-H.; Kumar, P.; Takenobu, T.; Li, L.-J. Hole Mobility Enhancement and p-doping in Monolayer WSe_2 by Gold Decoration. *2D Mater.* **2014**, *1* (3), No. 034001.
(47) Tsao, H.-W.; Kaun, C.-C.; Su, Y.-H. Decorating a WSe_2 Monolayer with Au Nanoparticles: A Study Combined First-Principles Calculation with Material Genome Approach. *Surf. Coat. Technol.* **2020**, *388*, No. 125563.
(48) Al-Johani, H.; Abou-Hamad, E.; Jedidi, A.; Widdifield, C. M.; Viger-Gravel, J.; Sangaru, S. S.; Gajan, D.; Anjum, D. H.; Ould-Chikh, S.; Hedhili, M. N.; et al. The Structure and Binding Mode of Citrate in the Stabilization of Gold Nanoparticles. *Nat. Chem.* **2017**, *9* (9), 890−895.
(49) Park, J.-W.; Shumaker-Parry, J. S. Structural Study of Citrate Layers on Gold Nanoparticles: Role of Intermolecular Interactions in Stabilizing Nanoparticles. *J. Am. Chem. Soc.* **2014**, *136* (5), 1907−1921.
(50) Zhao, X.; He, D.-W.; Wang, Y.-S.; Fu, C. In Situ Growth of Different Numbers of Gold Nanoparticles on MoS_2 with Enhanced Electrocatalytic Activity for Hydrogen Evolution Reaction. *Chin. Phys. B* **2018**, *27* (6), No. 068103.
(51) Wang, J.; Fang, W.; Hu, Y.; Zhang, Y.; Dang, J.; Wu, Y.; Zhao, H.; Li, Z. Different Phases of Few-Layer MoS_2 and Their Silver/Gold Nanocomposites for Efficient Hydrogen Evolution Reaction. *Catal. Sci. Technol.* **2020**, *10* (1), 154−163.
(52) Sahoo, P. K.; Bisoi, S. R.; Huang, Y.-J.; Tsai, D.-S.; Lee, C.-P. 2D-Layered Non-Precious Electrocatalysts for Hydrogen Evolution Reaction: Fundamentals to Applications. *Catalysts* **2021**, *11* (6), 689.
(53) Kim, J.-S.; Pyun, S.-I. Comparison of Transmissive Permeable and Reflective Impermeable Interfaces between Electrode and Electrolyte. *J. Solid State Electrochem.* **2011**, *15* (11), 2447−2452.
(54) Ardizzone, S.; Fregonara, G.; Trasatti, S. Inner" and "Outer" Active Surface of RuO_2 Electrodes. *Electrochim. Acta* **1990**, *35* (1), 263−267.
(55) Liu, C.; Gillette, E. I.; Chen, X.; Pearse, A. J.; Kozen, A. C.; Schroeder, M. A.; Gregorczyk, K. E.; Lee, S. B.; Rubloff, G. W. An All-in-One Nanopore Battery Array. *Nat. Nanotechnol.* **2014**, *9* (12), 1031−1039.
(56) Hirunpinyopas, W.; Iamprasertkun, P.; Fevre, L. W. L.; Panomsuwan, G.; Sirisaksoontorn, W.; Dryfe, R. A. W.; Songsasen, A.

Insights into binding mechanisms of size-selected graphene binders for flexible and conductive porous carbon electrodes. *Electrochim. Acta* **2022**, *403*, No. 139696.

(57) Duraisamy, S.; Ganguly, A.; Sharma, P. K.; Benson, J.; Davis, J.; Papakonstantinou, P. One-Step Hydrothermal Synthesis of Phase-Engineered MoS_2/MoO_3 Electrocatalysts for Hydrogen Evolution Reaction. *ACS Appl. Nano Mater.* **2021**, *4* (3), 2642−2656.

https://doi.org/10.1021/acs.inorgchem.4c02668
Inorg. Chem. 2024, 63, 18750−18762